Synsint Research Group

Available online at www.synsint.com

Synthesis and Sintering

ISSN 2564-0186 (Print), **ISSN** 2564-0194 (Online)

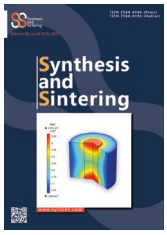

Research article

Numerical optimization of sample and die geometric parameters to increase the attainable temperature during spark plasma sintering of TiC ceramics

Saeed Mohammad Bagheri [a], **Mohsen Naderi** [a], **Mohammad Vajdi** [a,*], **Farhad Sadegh Moghanlou** [a,*], **Ali Tarlani Beris** [b]

[a] *Department of Mechanical Engineering, University of Mohaghegh Ardabili, Ardabil, Iran*
[b] *Department of Mechanical Engineering, College of Engineering, Boston University, Boston, USA*

ABSTRACT

The present study offers a comprehensive thermal modeling of spark plasma sintering (SPS) for a titanium carbide (TiC) sample. Utilizing COMSOL Multiphysics Software, the research investigates the temperature distribution within the TiC sample, situated within a graphite die. The study employs governing equations for heat diffusion, augmented by terms accounting for Joule heating, to calculate temperature variations. Boundary conditions, particularly at the upper and lower limits of the system, are explicitly accounted for, with cooling mechanisms modeled as convection. Through the application of the Taguchi method and Analysis of Variance (ANOVA), the study identifies the diameter of the sintering sample as the most significant parameter affecting the maximum temperature at the center of the TiC sample, with a significance of about 87%. The outer diameter of the graphite die followed with a significance of slightly more than 10%, and the thickness of the TiC sample had a significance of around 2%. The findings contribute to a nuanced understanding of the SPS process, offering valuable insights for optimizing the sintering parameters. Numerical results further underscore the importance of specific geometric parameters in the SPS process. This study serves as a robust foundation for future research aimed at refining the SPS process for TiC samples and other materials.

KEYWORDS

Titanium carbide
Spark plasma sintering
Taguchi method
Numerical analysis
Temperature distribution

OPEN ACCESS

1. Introduction

In the rapidly developing field of materials science, ultra-high-temperature ceramics (UHTCs) have emerged as a transformative class of materials, demonstrating exceptional resilience under extreme heat, specifically those exceeding 3000 °C [1, 2]. In addition to their excellent ability to conduct heat and resist oxidation, UHTCs have gained prominence in aerospace engineering applications, forming thermal protection systems for spacecraft and hypersonic vehicles and essential components in advanced propulsion mechanisms [3, 4]. However, the overall performance of UHTCs is not solely determined by their inherent material properties; it is also intricately influenced by the choice of fabrication methods [5]. While conventional techniques such as hot pressing (HP) have been fundamental, advanced techniques like spark plasma sintering (SPS) are changing performance standards. These fabrication methods significantly impact the resulting microstructure of UHTCs, thereby affecting critical performance parameters such as density, mechanical strength, and thermal properties

* Corresponding authors. *E-mail address:* vajdi@uma.ac.ir (M. Vajdi), f_moghanlou@uma.ac.ir (F. Sadegh Moghanlou)
Received 1 October 2023; Received in revised form 9 November 2023; Accepted 10 November 2023.

https://doi.org/10.53063/synsint.2023.34179

[6]. Consequently, ongoing research is focused on synergistically optimizing material attributes and fabrication techniques, positioning UHTCs as essential materials for future aerospace applications characterized by extreme conditions [3].

Sintering is a critical step in producing materials that need to have specific characteristics. As the tech world keeps moving forward, requiring quicker and more precise ways of doing things, SPS is coming into the spotlight as an upgrade over conventional sintering techniques [7]. The critical difference in SPS is how it goes about heating the material. Traditional sintering uses external heat, like ovens or furnaces, but SPS flips the script by using an electric current to create internal heat [8]. This happens when the electricity passes through the material itself. This inside-out heating approach leads to a faster and generally more even joining of particles. Speed is one of SPS's big selling points. The older sintering methods are often time-consuming, and keeping materials hot for a long time can mess with their structure. SPS gets the job done more quickly and usually at cooler temperatures, making it an excellent option for materials that didn't play well with older sintering techniques [9, 10].

To understand how SPS works, a detailed examination of its distinct methodology is required. Upon introduction of the material, commonly in powdered form, into the SPS apparatus, it is subjected to concurrent electrical and mechanical forces [11]. The electrical current traverses through the powdered material and encounters the innate resistance of the particles. This interaction generates heat via a process called "Joule heating." The generated heat facilitates the bonding of the particles [12]. Concurrently, mechanical pressure is exerted upon the material to enhance compaction. This synergistic application of both thermal and mechanical forces culminates in a final product characterized by high density and mechanical robustness, all while preserving the intended material properties. The electrical current is delivered in rapid, short pulses, contributing to accelerated heating rates. This expeditious heating inhibits any significant grain growth, thereby yielding a product with a refined microstructure [13].

Numerical methods play a significant role in SPS and field-activated sintering technology (FAST). These computational techniques provide nuanced insights into the sintering process and its variables, often surpassing the precision of experimental methods. With the advantages of handling larger datasets, reducing costs and time, and enhancing result accuracy, numerical simulations have become indispensable in SPS and FAST research. Critical parameters like temperature distributions, densification behaviors, and electrical nuances have been meticulously studied to optimize these methods. As technology advances, it is clear that computational approaches will continue to be a cornerstone in the evolution of SPS and FAST technologies [14–16].

Delving into the nuanced world of SPS, it's clear that this technique is paramount for advancing materials [17]. Various researchers have endeavored to demystify its processes and outcomes. Cincotti et al. [18] exploration stands out as they delve into the multifaceted physicochemical phenomena inherent to SPS. Their study, which particularly highlights configurations devoid of powders, sheds light on the intricate electrical dynamics involved. Emphasis is placed on the crucial role of the root mean square electric current in determining the Joule effect. Through their detailed analysis, resistances between stainless steel electrodes and graphite spacers are identified, with these resistances being influenced by temperature and mechanical variables. In stark contrast, horizontal resistances among graphite elements are negligible. Their model's accuracy is further confirmed when juxtaposed with diverse experimental data.

Olevsky et al. [19] further augment the understanding of SPS by introducing a comprehensive three-dimensional thermo-electro-mechanical model. This model, tested across different tooling sizes and temperature regimes, finds validation when its predictions align closely with experimental data. A salient takeaway from their research is the discernible impact of tooling size on the sample's heating patterns during SPS, pointing to the necessity of precise modeling, especially in industrial contexts.

In the realm of material-specific studies, Cheng et al. [20] delve into the nuances of TiC properties when subjected to SPS. Their data suggests that elevations in sintering temperature and holding time amplify the Vickers hardness (HV) and relative density of TiC. However, fracture toughness (KIC) appears largely resistant to these parameter changes. Remarkably, under specific conditions, namely sintering at 1600 °C for 5 minutes under a pressure of 50 MPa, the achieved HV nears 30.31 GPa with a density almost reaching 99.90%. Moreover, their investigations unveil a nuanced interplay between applied pressure, ensuing grain growth, and densification.

Complementing the material-centric studies, Babapoor et al. [21] concentrate on the implications of SPS temperature variations on TiC ceramic properties. Their experiments, spanning temperatures from 1800 to 2000 °C, indicate that 1900 °C emerges as the optimal sintering temperature. At this juncture, the TiC ceramic manifests a relative density of 99.4%, a Vickers hardness of 25.7 GPa, and a commendable thermal conductivity of 17.9 W/mK. However, any further increase in temperature to 2000 °C appears detrimental to these attributes. Their conclusion underscores the achievement of a fully-sintered TiC ceramic at 1900 °C without significant grain growth.

The primary objective of incorporating thermal models in SPS operations is to optimize temperature profiles within the TiC sample and the surrounding system. This process allows for greater control over sintering, resulting in a more refined microstructure [22, 23]. Given the critical role of SPS in the fabrication of UHTCs, this research focuses on a numerical exploration of temperature variations during the spark plasma sintering of titanium carbide ceramics. TiC, a UHTC, has been the subject of extensive research due to its extraordinary features, such as high melting point, low density, and unique chemical and thermal properties [24]. Understanding temperature gradients is essential, as they directly impact the final microstructure and mechanical attributes of the sintered product. This study employs Finite Element Analysis (FEA) to tackle the complex interplay between thermal and electrical factors intrinsic to the sintering process. To enrich the scope and precision of this research, the Taguchi method is utilized along with Sensitivity analysis, concentrating on how changes in dimensions like die diameter, sample height, and sample diameter affect temperature distributions.

2. Methodology

2.1. Design of experiments

When researchers are dealing with many parameters in the design of experiments and each parameter consists of different levels, they face many problems in performing all the experiments that can find the best performance and the most optimal state. Conducting consecutive tests in multiple conditions is not only time-consuming but also requires

spending a lot of money. Taguchi method is one of the best solutions to overcome this problem and get rid of multiple tests. This method is very user-friendly and uses orthogonal arrays for optimization purposes. By processing the data in a statistical way, with the assistance of this method, interesting results can be extracted from the limited findings. In fact, this method helps the researcher to clarify the role and importance of parameters and determine the significance of each input parameter on the efficiency of output results. Another advantage of this method is to predict the optimal state in such a way that the efficiency of the output parameter is as high as possible [25, 26].

In general, the Taguchi method divides the quality characteristics into 3 classes: “nominal is better”, “lower is better”, or “higher is better” [27]. The purpose of this research is to simulate the spark plasma sintering process of TiC ceramics by keeping the applied electric current constant and the optimization of some geometric parameters with the aim of achieving the maximum temperature at the center of the sample. For this aim, the outer diameter of the graphite die, the diameter of the sintered sample that equals the inner diameter of the graphite die, and the thickness of the sintered sample are examined as the input parameters. Since the goal of this work is to reach a higher temperature with minimum standard deviations of temperature in different directions of the sample, the qualitative characteristics are included in Table 1. Qualitek-4 software is used for experimental design and statistical analysis of results.

As mentioned, the significance of the outer diameter of the die, the diameter of the sample, and the thickness of the sample on the maximum temperature attainable at the center of the sample are determined. Although in the design of the experiment, any number can be considered for the parameter levels, the range of logical values can be guessed to some extent by reading the previously published literature [28, 29]. Thus, the selected levels for these three parameters are provided in Table 2. In traditional full factorial experimental design, if 3 parameters are defined in 3 levels, 27 experiments are needed. If the Taguchi method and orthogonal arrays (L9 in this case) are considered, the number of experiments is reduced to 9, which are presented in Table 3. After performing 9 runs suggested by this method, analysis of variance (ANOVA) is used to determine the importance and contribution of each input parameter on the maximum achievable temperature.

2.2. Geometry

In the current study, thermal modeling of spark plasma sintering for TiC sample was conducted utilizing COMSOL Multiphysics Software. As depicted in Fig. 1, the setup comprises a TiC powder sample situated within a graphite die, accompanied by graphite punches at both the superior and inferior positions. Inconel elements at the terminal sections function as cooling agents and interface with a water circulation system, maintained at a uniform temperature of 300 Kelvins. The dimensions of the variable parameters shown in Fig. 2 are specified in Table 3. Additionally, other geometric dimensions are parametrically represented by the variable L.

Table 1. Analyzed output parameters and their logical quality characteristics.

Output parameter	Quality characteristic
Temperature of the sample center	Higher is better
Standard deviation of temperature	Lower is better

Table 2. Studied geometric parameters and chosen levels.

Parameter	Level 1	Level 2	Level 3
Outer diameter of the die (mm)	60	80	100
Diameter of the sample (mm)	25	35	45
Thickness of the sample (mm)	3	6	9

2.3. Governing equations and Boundary condition

In the study, the temperature distribution within the sample was calculated by solving the governing equation for heat diffusion, which was augmented by a term to account for heat generated via Joule heating. Given the axisymmetric nature of the assembly, the equation can be simplified. The equation is expressed as follows in Eq. 1 [29]:

$$\gamma c_p \frac{\partial T}{\partial t} = \frac{1}{r}\frac{\partial}{\partial r}(r\lambda_r \frac{\partial T}{\partial r}) + \frac{\partial}{\partial z}(\lambda_z \frac{\partial T}{\partial z}) + q_i \quad (1)$$

In Eq. 1, the variables γ , λ_r and λ_z represent the material density and thermal conductivities in the radial (r) and axial (z) directions, respectively. The variable C_P stands for the specific heat capacity of the material, t is time, T is the temperature at a given location within the sample, and q_i represents the rate of heat generation per volume per time due to Joule heating.

By solving this equation, one can attain a spatial and temporal profile of the temperature within the sample. This is essential for understanding the thermal behavior of the system under study. The mathematical formulation is based on an axisymmetric assumption, simplifying the computational complexity involved in its solution. As such, it offers a practical yet accurate approach to studying thermal phenomena in systems that are symmetric about an axis.

The equation for current distribution in a cylindrical system is formulated in accordance with Kirchhoff’s junction rule, as indicated by Eq. 2 [28]:

$$\frac{1}{r}\frac{\partial(r i_r)}{\partial r} + \frac{\partial(i_z)}{\partial z} = 0 \quad (2)$$

Table 3. The applied L9 orthogonal array for the numerical investigation, geometric dimensions in mm.

Run No.	Outer diameter of the die (d1)	Diameter of the sample (d2)	Thickness of the sample (z)
1	60	25	3
2	60	35	6
3	60	45	9
4	80	25	6
5	80	35	9
6	80	45	3
7	100	25	9
8	100	35	3
9	100	45	6

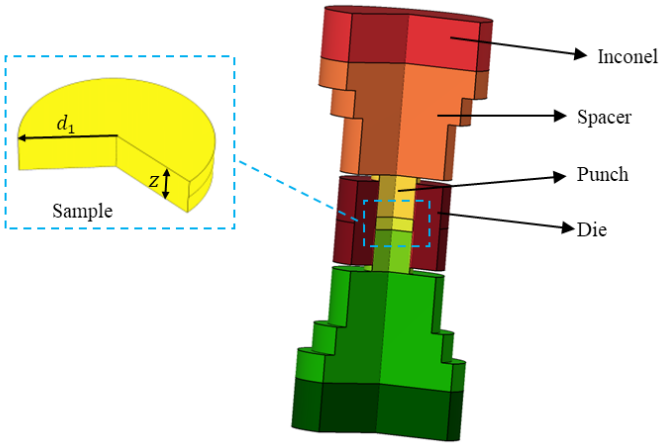

Fig. 1. The schematic of the SPS setup.

Within this equation, the variables i_r and i_z specifically denote the current densities in the radial (r) and axial (z) directions, respectively.
The Root-Mean-Square (RMS) values for both voltage and current intensity are essential metrics for assessing the power dissipation within the heating tools. Eq. 3 mathematically defines the RMS value of the voltage [30].

$$U_{RMS} = \sqrt{\frac{1}{P}\int_{t-T}^{t} u^2(\tau)d\tau} \quad (3)$$

In the above equation, the symbol *u* represents the instantaneous voltage applied to the sample, and T denotes the period of the alternating current (AC).

Heat conduction at the upper and lower boundaries of the system is explicitly accounted for in the model. These boundaries are subjected to cooling by water, and the heat transfer mechanism is modeled as convection. Eq. 4 outlines the boundary condition applied:

$$q_{conv} = h(T_p - T_w) \quad (4)$$

where h is the convection coefficient, assumed to be 880 W/m^2.K [31]. Additionally, T_p and T_w represent the wall surface temperature and water temperature (set at 300 K), respectively.
Radiative heat transfer at the vertical walls of the die, punches, spacer, and electrodes is governed by the Stefan-Boltzmann law, as described in Eq. 5:

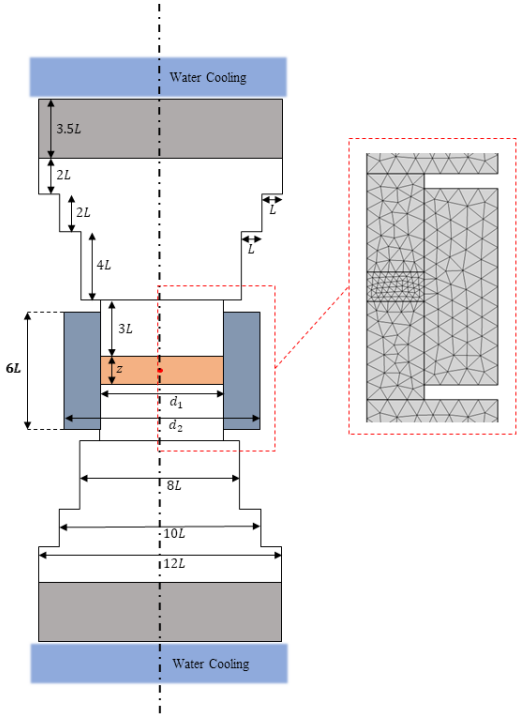

Fig. 2. The sample and die geometry and a sample of mesh at the die, punch, and sample.

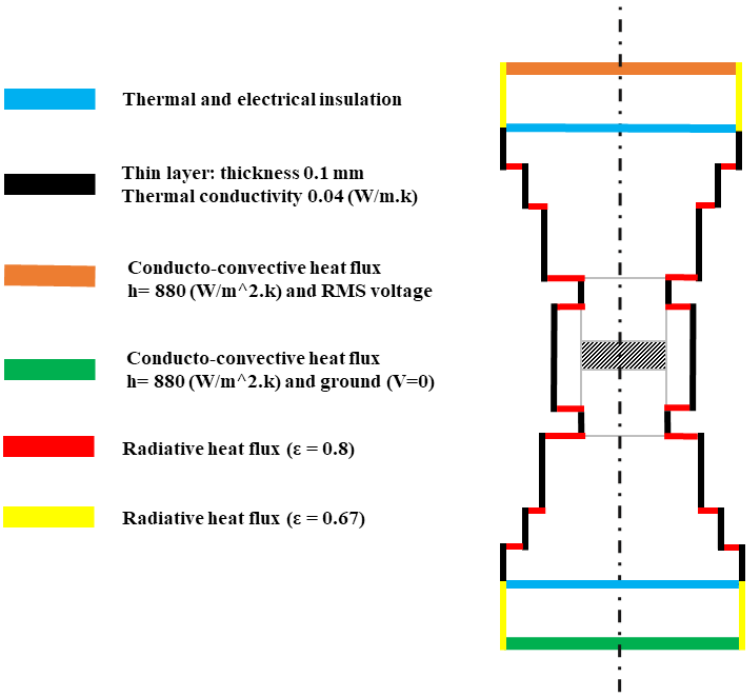

Fig. 3. Encapsulated overview of boundary conditions

$$q_r = \sigma_s \varepsilon (T_e^4 - T_a^4) \quad (5)$$

In this equation, q_r is the radiative heat flux, σ_s is the Stefan-Boltzmann constant, ε denotes the emissivity values (0.67 for Inconel [32] and 0.8 for graphite [19]), T_e signifies the emission temperature, and T_a represents the chamber wall temperature.

Additionally, electrical, and thermal contact resistances (ECR and TCR, respectively) are modeled through the use of interfacial graphite/graphite conditions between the spacers and punches. The electrical and thermal fluxes at this interface are expressed in Eqs. 6 and 7, respectively:

$$J_{el} = \sigma_c (U_c - U_p) \quad (6)$$

$$q_{th} = k_c (T_s - T_p) \quad (7)$$

where, σ_c and k_c stand for the electrical and thermal gap conductivity, respectively. (U_c-U_p) and (T_s-T_p) are the potential and temperature differences between the spacer and the punch, respectively.

Following the detailed exposition of the differential governing equations, specific boundary conditions are required for comprehensive SPS modeling. The outer surfaces of the assembly interact with ambient air at a stable temperature of 300 K, which induces natural convection with the stationary air in the immediate surroundings. Additionally, radiative heat transfer between these exterior surfaces and the ambient environment is incorporated into the model. The electrical potential at both electrode interfaces is initialized at zero. Convective heat transfer is accounted for at the upper and lower system boundaries. The applied RMS voltage, which is time-dependent, serves to mirror the fluctuating potential typically experienced during thermal processing. Given the extreme temperatures generated at the interfaces between Inconel and the spacers, as cited in recent research, active cooling of the system is essential.

Continuity in both thermal and electrical properties is assumed across different elements of the system. A thin layer, with a thickness of 0.1 mm and thermal conductivity of 0.04 W/m^2.K [32], is used to model the thermal contact resistance between Inconel and the spacer. As for the Electrical Contact Resistance (ECR), it is deemed negligible due to the large interface area and minimal current density and heat dissipation, as corroborated by the findings of Manière et al. [32]. In their experimental work, Manière et al. observed a reduction in ECR with elevated temperatures, becoming nearly insignificant at temperatures exceeding 800 °C and pressures above 100 MPa. Given that the sintering process for TiC operates in conditions around 100 MPa and 2000 °C, the ECR can be safely disregarded [19]. A detailed overview of the boundary conditions is encapsulated in Fig. 3.

To ensure mesh independence in the numerical analysis, various mesh configurations comprising different sizes and shapes were evaluated. Ultimately, a mesh consisting of 1,904 triangular elements was selected as it satisfied the criteria for mesh independence. A representative depiction of the meshed geometry is provided in Fig. 2. Owing to the elevated current density observed in the sample and the adjacent die, a finer mesh was employed in these regions to capture the nuances of the behavior more accurately.

2.4. Material properties

The apparatus comprises multiple components fabricated from diverse materials, each with specific properties that need to be input into the COMSOL Multiphysics. Both thermal and electrical attributes of the constituent materials namely Inconel, graphite, and titanium carbide are modeled as functions of temperature. A summary of these material properties is available in Table 4. For this simulation, all elements within the assembly are assumed to exhibit isotropic behavior.

Table 4. Summary of the material's properties.

Material	Heat capacity (J/kg.K)	Density (kg/m^3)	Thermal conductivity (W/m.K)	Electrical resistivity (Ωm)
Inconel [30]	$334+2.5\times10^{-1}$ T	8430	$10.1+1.57\times10^{-2}$ T	$9.82\times10^{-7}+1.6\times10^{-10}$ T
Graphite [32]	$34.27+2.72$ T-9.6×10^{-4} T^2	$1904-1.41\times10^{-2}$ T	$123-6.99\times10^{-2}$ T$+1.55\times10^{-5}$ T^2	$1.7\times10^{5}-1.87\times10^{8}$ T-1.26×10^{11} T$^2-2.44\times10^{15}$ T^3
TiC	$803+5.744\times10^{-2}$ T-5.427×10^{-5} T$^2-23.685\times10^{6}$/T^2 [33]	4930 [34]	9.8×10^{-3} T$+23.994$ [35]	$1/(6\times10^{-10}$ T$+4\times10^{-7})$ [35]

3. Results and discussion

In the study at hand, computational analysis was conducted on the SPS of the TiC sample. To validate the accuracy of the findings, temperature measurements from the core of the sample to the end of the die were cross-referenced with the research data published by Bagheri et al. [28]. By replicating the conditions specified in Bagheri's study, the sintering behavior of TiC was modeled. The outcomes, illustrated in Fig. 4, confirm the reliability of the employed computational approach. Therefore, the developed simulation can be used to model the SPS of TiC at different geometrical conditions suggested by the Taguchi method, as shown in Table 3. All runs have been conducted, and the temperature distribution in the geometry is obtained. Fig. 5 and Fig. 6 show the temperature contours in the sample for runs No. 1 and No. 9, while Fig. 7 and Fig. 8 demonstrate the temperature contours in the whole mesh geometry for runs No. 1 and No. 9.

It can be concluded that temperature distribution in the axial direction is almost uniform for the sample, as the target region is supposed to have the maximum and uniform temperature, while temperature distribution has lost its uniformity in the radial direction, which has an essential role in the grid size of the final product.

The maximum temperature calculated numerically for the center of each sample during the sintering process is reported in Table 5. Additionally, the standard deviations of temperature changes in the radial direction from the center of the sample to the periphery and also in the axial direction are presented in the same table. The sintered sample in run No. 7 shows the lowest temperature of 1768.0 °C. The highest temperature of 2096.9 °C is obtained for the sintered sample in run No. 3. Although all the samples are sintered by applying the same electric current, a temperature difference of about 330 °C can be observed between them. The grand average of the temperatures of all samples' centers is 1957.1 °C. It is worth mentioning that the standard deviation of the calculated temperature of 9 samples equals 112.5 °C. It seems that such a temperature is sufficient to densify monolithic TiC ceramics without sinter additives. However, without taking into account other sintering parameters such as applied pressure and soaking time, it is not possible to express a definite opinion about complete sintering and full densification. The standard deviation of

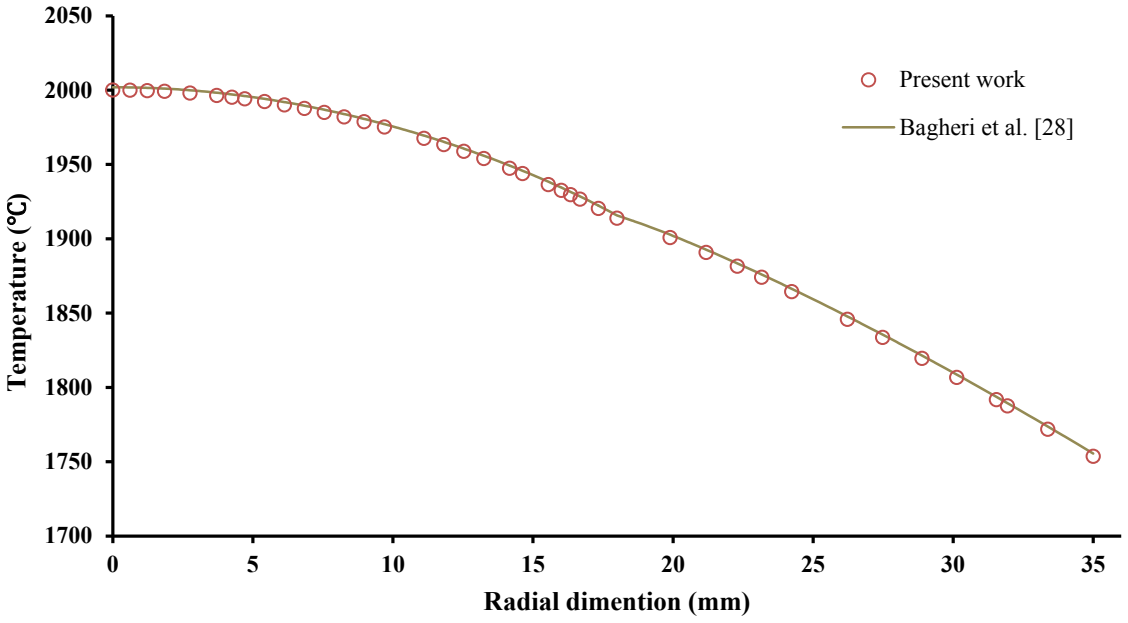

Fig. 4. The comparison of the temperature distribution at the center-to-outer surface of the sample and die between current work and Bagheri et al. [28].

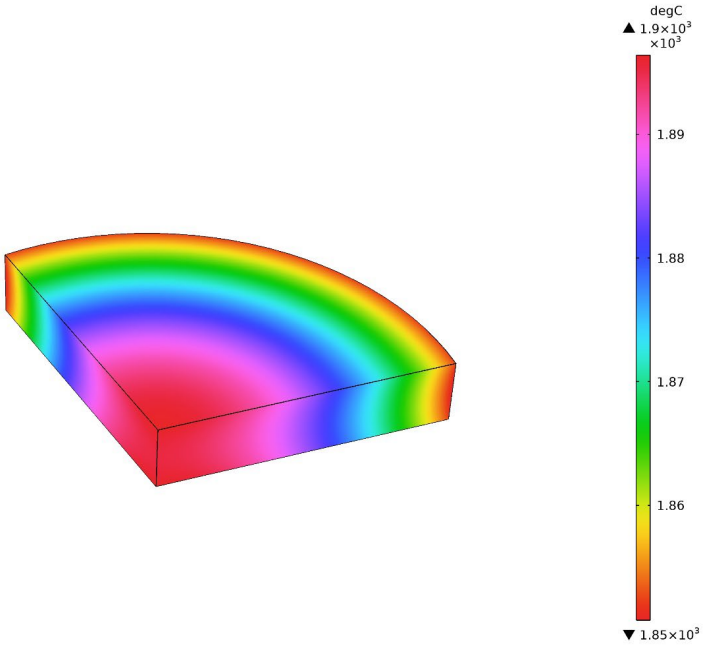

Fig. 5. Temperature contour in the sample for run No. 1.

temperature changes in the axial direction is very low and almost insignificant. Although the standard deviation of temperature changes in the radial direction is more significant than in the axial direction, in general, due to the high maximum sintering temperatures, such deviations can be considered minor. Fig. 9 depicts the main effect plots of mean values for the temperature of the TiC sample center. With the increase of the outer diameter of the graphite die from 60 mm to 80 mm and then from 80 mm to 100 mm, the average temperature of the center of the sample decreases from 2004.8 °C to 1942.5 °C and then to 1924.1 °C. As can be seen, the average temperature drop in the first step is much higher than in the second step. If the diameter of the pellet-shaped sample increases from

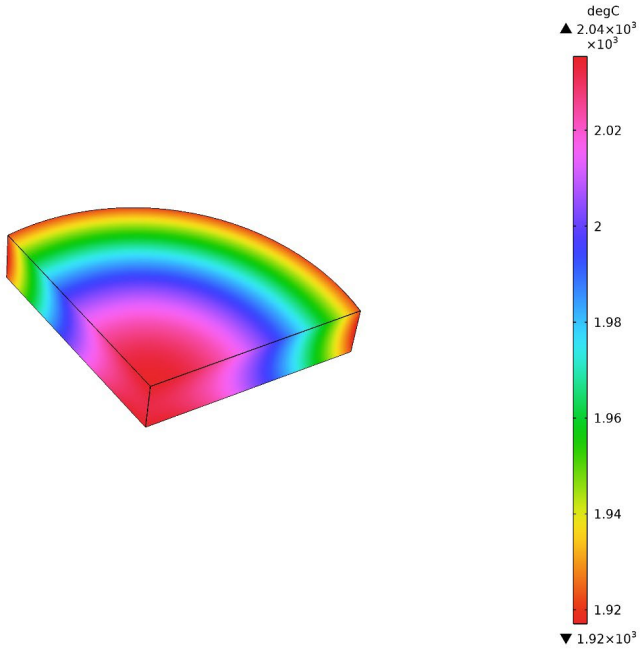

Fig. 6. Temperature contour in the whole die-sample-punch geometry for run No. 9.

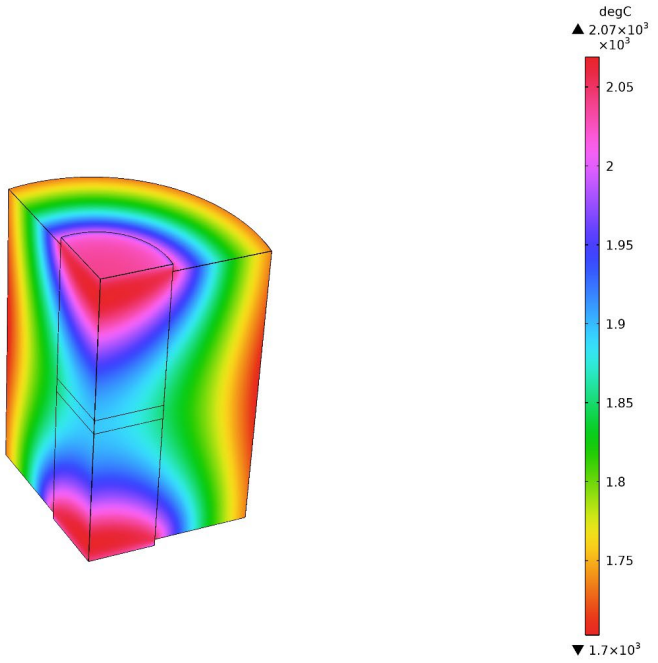

Fig. 7. Temperature contour in the whole die-sample-punch geometry for run No. 1.

25 mm to 35 mm, the average temperature of its center elevates sharply from 1826.0 °C to 1980.9 °C. A difference of 155 °C in the mean temperature of the center of two samples, which have only a 5 mm difference in radius, is very impressive and remarkable. If the diameter of the sample is increased more to 45 mm, the average temperature of the center of the sample rises from 1980.9 °C to 2064.5 °C. Although the intensity of the temperature enhancement in this step is less than the previous one, such an increase in temperature around 85 °C is also considerable. Therefore, it seems that the diameter of the sample compared to the outer diameter of the die has a much greater effect on

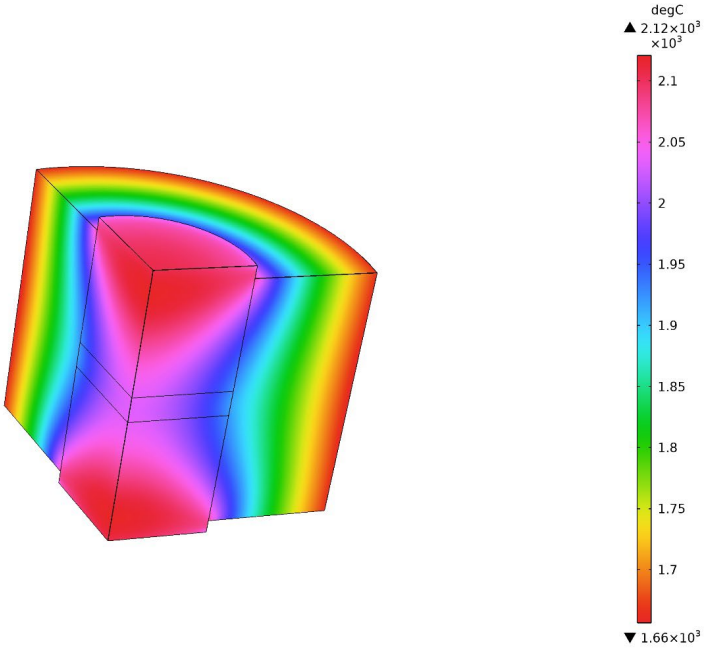

Fig. 8. Temperature contour in the whole die-sample-punch geometry for run No. 9.

Table 5. Output parameters obtained by numerical method.

Run No.	Temperature of the sample center (°C)	Standard deviation of temperature in radial direction (°C)	Standard deviation of temperature in axial direction (°C)
1	1895.3	14.8	0.4
2	2022.3	28.0	1.4
3	2096.9	43.6	2.7
4	1814.7	13.8	1.7
5	1947.9	25.5	3.5
6	2064.9	36.4	0.3
7	1768.0	13.8	4.0
8	1972.4	26.3	0.4
9	2031.8	38.2	1.2
Grand average	1957.1		
Standard deviation	112.5		

achieving the maximum temperature in the center of the sample. Regarding the effect of the sample thickness on the mean temperature in its center, it appears that there is an almost linear decreasing behavior. In other words, as the thickness increases from 3 mm to 6 mm and then 9 mm, the average temperature in the center of the sample drops from 1977.5 °C to 1956.3 °C and then to 1937.6 °C. By comparing the trend of average temperature changes affected by three input parameters, it can be concluded that the thickness of the sample has the least influence on the mean temperature of the sample center.

The ANOVA outcomes of the analyzed parameters on the temperature of the TiC sample center are reported in Table 6. Not only the degree of freedom of each of the three investigated input parameters is equal to 2, but the degree of freedom of the other/error is also calculated to be 2. Calculations related

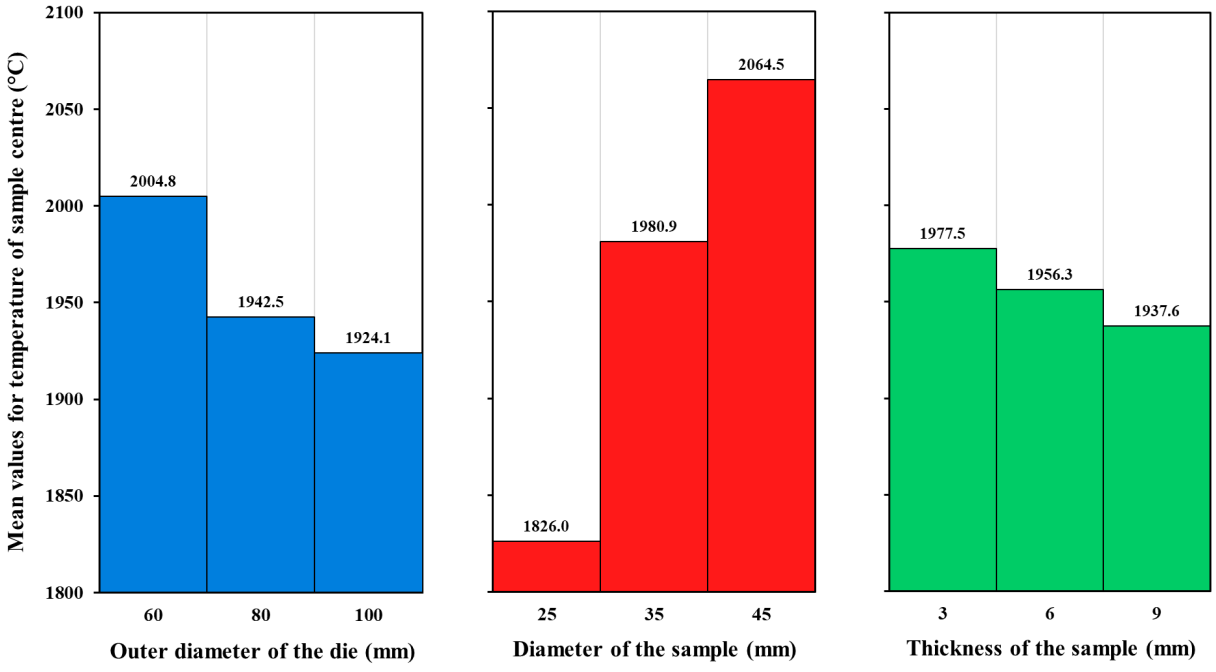

Fig. 9. Main effect plots of mean values for the temperature of the sample center.

Table 6. ANOVA data of analyzed parameters on the temperature of the sample center.

Parameter	Degrees of freedom	Sum of squares	Variance	F-ratio	Pure sum	Significance (%)
Outer diameter of die	2	10750.388	5375.194	74.253	10605.608	10.482
Diameter of sample	2	87880.911	43940.455	606.996	87736.131	86.721
Thickness of sample	2	2394.433	1197.216	16.538	2249.653	2.223
Other/error	2	144.779	72.389	-	-	0.574
Total	8	101170.513	-	-	-	100.000

to statistical terms, including sum of squares, variance, F-ratio, and pure sum are also reported in this table; of course, significance is the most important value. Based on ANOVA, the diameter of the sintering sample is recognized as the most important input parameter affecting the maximum temperature of the TiC sample center with a significance of about 87%. The second place is the importance of the outer diameter of the graphite die, and its significance value is slightly more than 10%. The least important input parameter among the investigated parameters in this research is the thickness of the TiC sample, the significance of which is around 2%. The importance of errors or unknown parameters is calculated below 1%, which is insignificant.

For a better graphical understanding of the significance of all parameters, a relevant pie chart is shown in Fig. 10. The red area which occupies a large part of this chart corresponds to the diameter of the sintering sample. Therefore, it seems that within the range of levels chosen for the parameters in this research, the diameter of the TiC ceramic sample, which is considered from 25 mm to 45 mm, is very effective on the maximum temperature of the sample center compared to other items. However, the range chosen for the outer diameter of the graphite mo die (60–100 mm) is not unimportant and affects the total significance by about 10%. Since the thickness range defined for the sintering sample has a significance of ~2%, it can be claimed that the changes in the thickness of the sample from 3 mm to 9 mm do not have much effect on the maximum temperature of the center of the TiC sample. Therefore, there is no need to control or spend a lot of sensitivity on the thickness of the sample from this point of view.

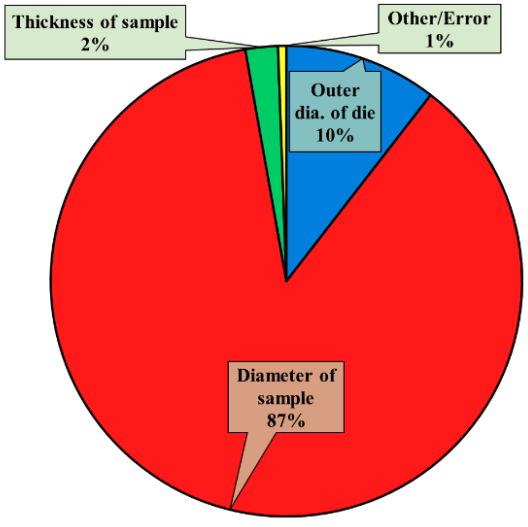

Fig. 10. Significance pie chart of analyzed parameters on the temperature of the sample center.

Table 7 presents the contributions of all analyzed parameters on the maximum temperature of the TiC sample center in optimal conditions. Based on this approach, if level 1 is considered for the outer diameter of the graphite die, 60 mm, its contribution is 47.7 °C. The maximum contribution of 107.4 °C is obtained when the diameter of the TiC sample being sintered is selected at level 3 or 45 mm. If 3 mm (level 1) is chosen for the thickness of the TiC sample, a contribution of 20.4 °C can be achieved. Therefore, the total contributions of all input parameters is 175.5 °C in the optimal state. This means that if all the parameters are considered at their optimal level, 175.5 °C is added to the average value of the maximum temperature of the center of the sample. As a result, with the assumption of the 1957.1 °C grand average for the maximum temperature of the TiC sample in its center, as reported in Table 7, a temperature of 2132.6 °C is predicted for the maximum temperature of the center of the sample in optimal state.

To assess the expected value, a new verification run is performed in the optimal conditions, mentioned in Table 7, with the help of Comsol Multiphysics software, in which the electric current is assumed to be the same as the previous 9 runs. By simulation

Table 7. Contribution of analyzed parameters on the temperature of the sample center.

Parameter	Level	Level description	Contribution (°C)
Outer diameter of die	1	60 mm	47.7
Diameter of sample	3	45 mm	107.4
Thickness of sample	1	3 mm	20.4
Total contributions			175.5
Grand average			1957.1
Expected temperature at optimal condition			2132.6

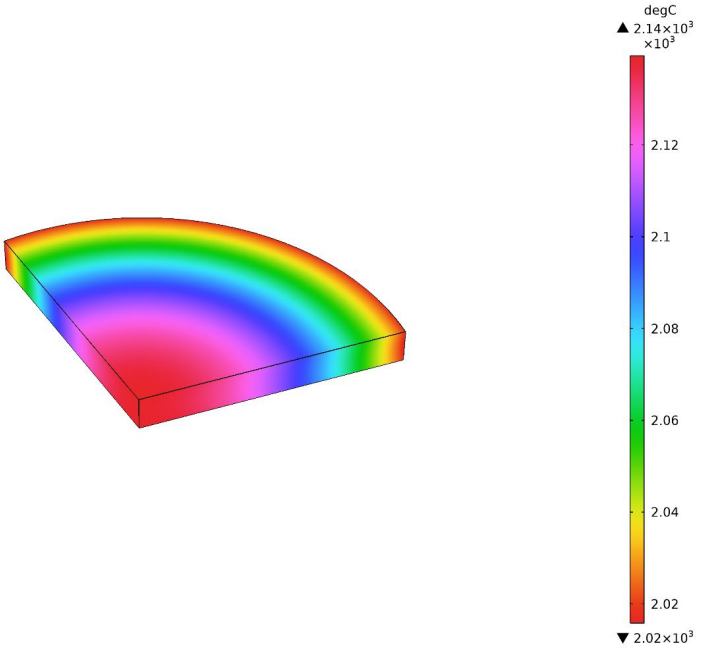

Fig. 11. Temperature contour in the whole die-sample-punch geometry for the optimum conditions obtained by the Taguchi method.

and numerical analysis on a TiC sample with a diameter of 45 mm and a thickness of 3 mm that is sintered inside a graphite die with an outer diameter of 60 mm, the maximum temperature in its center is computed to be 2138.7 °C. The temperature contours for the suggested optimal geometry are shown in Fig. 11 and Fig. 12 for the sample and whole meshed domain, respectively, as a verification run. Surprisingly, this number (2138.7 °C) is very close to the predicted value of 2132.6 °C. It is worth noting that the temperature difference of 6 °C at a very high temperature of about 2100 °C is extremely insignificant and can be ignored. Hence, with an excellent approximation, the prediction of Taguchi's model can be considered valid.

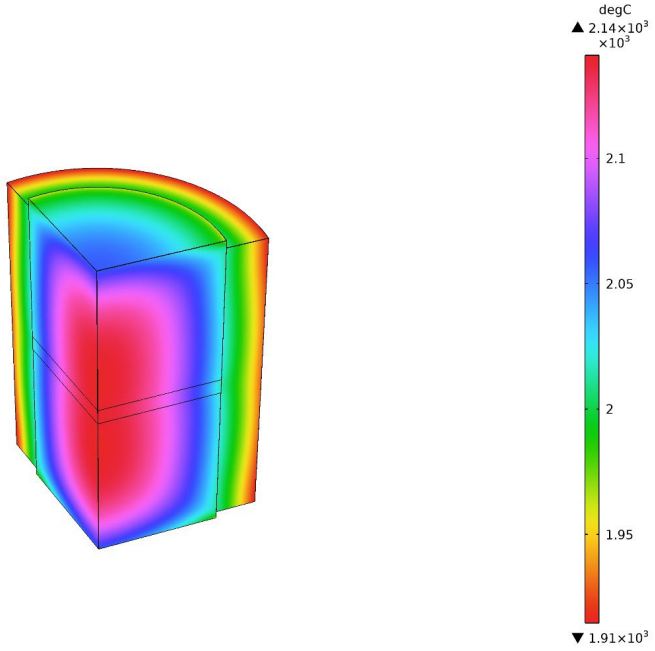

Fig. 12. Temperature contour in the whole die-sample-punch geometry for the optimum conditions obtained by the Taguchi method.

4. Conclusions

This study offers a robust thermal model for spark plasma sintering of titanium carbide using Finite Element Analysis and the Taguchi method. Key findings indicate the diameter of the sintering sample as the most impactful parameter, with an 87% significance level. Lesser influences include the graphite die's outer diameter and TiC sample thickness, with 10% and 2% significance, respectively. Using the Taguchi method streamlined the experimental design from 27 to 9 tests, enhancing efficiency, while ANOVA results validated the model's robustness, showing negligible error below 1%. Future work should focus on empirical validation and parameter expansion.

CRediT authorship contribution statement

Saeed Mohammad Bagheri: Data curation.
Mohsen Naderi: Software, Writing – original draft.
Mohammad Vajdi: Conceptualization, Supervision, Writing – review & editing.
Farhad Sadegh Moghanlou: Project administration, Supervision, Writing – review & editing.
Ali Tarlani Beris: Validation, Software.

Data availability

The data underlying this article will be shared on reasonable request to the corresponding author.

Declaration of competing interest

The authors declare no competing interests.

Funding and acknowledgment

The authors gratefully acknowledge the University of Mohaghegh Ardabili for the support of this research. The resources provided by Boston University have been pivotal in the realization of this work. These supports have significantly contributed to the successful completion of this study and are deeply acknowledged by the authors.

References

[1] W.G. Fahrenholtz, G.E. Hilmas, Ultra-high temperature ceramics: Materials for extreme environments, Scr. Mater. 129 (2017) 94–99. https://doi.org/10.1016/j.scriptamat.2016.10.018.
[2] B.R. Golla, A. Mukhopadhyay, B. Basu, S.K. Thimmappa, Review on ultra-high temperature boride ceramics, Prog. Mater. Sci. 111 (2020) 100651. https://doi.org/10.1016/j.pmatsci.2020.100651.
[3] J.-F. Justin, A. Julian-Jankowiak, V. Guérineau, V. Mathivet, A. Debarre, Ultra-high temperature ceramics developments for hypersonic applications, CEAS Aeronaut. J. 11 (2020) 651–664. https://doi.org/10.1007/s13272-020-00445-y.
[4] M. Sakkaki, S.M. Arab, In-situ synthesized phases during the spark plasma sintering of g-C3N4 added TiB2 ceramics: A thermodynamic approach, Synth. Sinter. 3 (2023) 73–78. https://doi.org/10.53063/synsint.2023.32151.
[5] S. Tang, C. Hu, Design, preparation and properties of carbon fiber reinforced ultra-high temperature ceramic composites for aerospace applications: A review, J. Mater. Sci. Technol. 33 (2017) 117–130. https://doi.org/10.1016/j.jmst.2016.08.004.
[6] R. Orrù, G. Cao, Comparison of reactive and non-reactive spark plasma sintering routes for the fabrication of monolithic and composite ultra high temperature ceramics (UHTC) materials, Materials (Basel). 6 (2013) 1566–1583. https://doi.org/10.3390/ma6051566.
[7] W.R. Matizamhuka, Spark plasma sintering (SPS) - an advanced sintering technique for structural nanocomposite materials, J. South. Afr. Inst. Min. Metall. 116 (2016) 1171–1180. https://doi.org/10.17159/2411-9717/2016/v116n12a12.
[8] S.-X. Song, Z. Wang, G.-P. Shi, Heating mechanism of spark plasma sintering, Ceram. Int. 39 (2013) 1393–1396. https://doi.org/10.1016/j.ceramint.2012.07.080.
[9] M. Shahedi Asl, Z. Ahmadi, S. Parvizi, Z. Balak, I. Farahbakhsh, Contribution of SiC particle size and spark plasma sintering conditions on grain growth and hardness of TiB2 composites, Ceram. Int. 43 (2017) 13924–13931. https://doi.org/10.1016/j.ceramint.2017.07.121.
[10] X.C. Zhong, S.M. Wu, X.T. Dong, Y.X. Li, J.H. Huang, et al., High density La-Fe-Si based magnetocaloric composites with excellent properties produced by spark plasma sintering, Mater. Sci. Eng. B. 280 (2022) 115717. https://doi.org/10.1016/j.mseb.2022.115717.
[11] M. Tokita, Progress of spark plasma sintering (SPS) method, systems, ceramics applications and industrialization, Ceramics. 4 (2021) 160–198. https://doi.org/10.3390/ceramics4020014.
[12] A.D. Preston, K. Ma, Effect of powder morphology on the microstructure and mechanical property gradients in stainless steels induced by thermal gradients in spark plasma sintering, MRS Adv. 6 (2021) 482–488. https://doi.org/10.1557/s43580-021-00089-y.
[13] W. Weifeng, X. Kuangdi, Spark plasma sintering, The ECPH Encyclopedia of Mining and Metallurgy, Springer Nature Singapore, Singapore. (2023) 1–2. https://doi.org/10.1007/978-981-19-0740-1_1127-1.
[14] J. Diatta, G. Antou, N. Pradeilles, A. Maître, Numerical modeling of spark plasma sintering—Discussion on densification mechanism identification and generated porosity gradients, J. Eur. Ceram. Soc. 37 (2017) 4849–4860. https://doi.org/10.1016/j.jeurceramsoc.2017.06.052.
[15] M. Fattahi, M. Najafi Ershadi, M. Vajdi, F. Sadegh Moghanlou, A. Sabahi Namini, M. Shahedi Asl, On the simulation of spark plasma sintered TiB2 ultra high temperature ceramics: A numerical approach, Ceram. Int. 46 (2020) 14787–14795. https://doi.org/10.1016/j.ceramint.2020.03.003.
[16] X.Y. Li, Z.H. Zhang, X.W. Cheng, G.J. Huo, S.Z. Zhang, Q. Song, The development and application of spark plasma sintering technique in advanced metal structure materials: A review, Powder Metall. Met. Ceram. 60 (2021) 410–438. https://doi.org/10.1007/s11106-021-00254-w.
[17] P. Cavaliere, B. Sadeghi, A. Shabani, Spark plasma sintering: process fundamentals, in: Spark Plasma Sinter. Mater., Springer International Publishing, Cham. (2019) 3–20. https://doi.org/10.1007/978-3-030-05327-7_1.
[18] A. Cincotti, A.M. Locci, R. Orrù, G. Cao, Modeling of SPS apparatus: Temperature, current and strain distribution with no powders, AIChE J. 53 (2007) 703–719. https://doi.org/10.1002/aic.11102.
[19] E.A. Olevsky, C. Garcia-Cardona, W.L. Bradbury, C.D. Haines, D.G. Martin, D. Kapoor, Fundamental aspects of spark plasma sintering: II. finite element analysis of scalability, J. Am. Ceram. Soc. 95 (2012) 2414–2422. https://doi.org/10.1111/j.1551-2916.2012.05096.x.
[20] L. Cheng, Z. Xie, G. Liu, W. Liu, W. Xue, Densification and mechanical properties of TiC by SPS-effects of holding time, sintering temperature and pressure condition, J. Eur. Ceram. Soc. 32 (2012) 3399–3406. https://doi.org/10.1016/j.jeurceramsoc.2012.04.017.
[21] A. Babapoor, M. Shahedi Asl, Z. Ahmadi, A.S. Namini, Effects of spark plasma sintering temperature on densification, hardness and

thermal conductivity of titanium carbide, Ceram. Int. 44 (2018) 14541–14546. https://doi.org/10.1016/j.ceramint.2018.05.071.
[22] D. Garbiec, V. Leshchynsky, A. García-Junceda, R. Swadźba, P. Siwak, et al., Microstructure and mechanical properties of spark plasma sintered and severely deformed AA7075 alloy, Metals (Basel). 11 (2021) 1433. https://doi.org/10.3390/met11091433.
[23] S. Jafargholinejad, S. Soleymani, Effects of carbon nano-additives on characteristics of TiC ceramics prepared by field-assisted sintering, Synth. Sinter. 1 (2021) 62–68. https://doi.org/10.53063/synsint.2021.1123.
[24] A. Sabahi Namini, Z. Ahmadi, A. Babapoor, M. Shokouhimehr, M. Shahedi Asl, Microstructure and thermomechanical characteristics of spark plasma sintered TiC ceramics doped with nano-sized WC, Ceram. Int. 45 (2019) 2153–2160. https://doi.org/10.1016/j.ceramint.2018.10.125.
[25] M. Naderi, M. Vajdi, F. Sadegh Moghanlou, H. Nami, Sensitivity analysis of fluid flow parameters on the performance of fully dense ZrB2-made micro heat exchangers, Synth. Sinter. 3 (2023) 88–106. https://doi.org/10.53063/synsint.2023.32143.
[26] M. Naderi, M. Vajdi, F. Sadegh Moghanlou, H. Nami, Numerical assessment of ceramic micro heat exchangers working with nanofluids by Taguchi optimization approach, Synth. Sinter. 3 (2023) 166–178. https://doi.org/10.53063/synsint.2023.33169.
[27] N.J. Rathod, M.K. Chopra, U.S. Vidhate, N.B. Gurule, U.V. Saindane, Investigation on the turning process parameters for tool life and production time using Taguchi analysis, Mater. Today Proc. 47 (2021) 5830–5835. https://doi.org/10.1016/j.matpr.2021.04.199.
[28] S. Mohammad Bagheri, M. Vajdi, F. Sadegh Moghanlou, M. Sakkaki, M. Mohammadi, et al., Numerical modeling of heat transfer during spark plasma sintering of titanium carbide, Ceram. Int. 46 (2020) 7615–7624. https://doi.org/10.1016/j.ceramint.2019.11.262.
[29] M. Sakkaki, F. Sadegh Moghanlou, M. Vajdi, M. Shahedi Asl, M. Mohammadi, M. Shokouhimehr, Numerical simulation of heat transfer during spark plasma sintering of zirconium diboride, Ceram. Int. 46 (2020) 4998–5007. https://doi.org/10.1016/j.ceramint.2019.10.240.
[30] A. Pavia, L. Durand, F. Ajustron, V. Bley, G. Chevallier, et al., Electro-thermal measurements and finite element method simulations of a spark plasma sintering device, J. Mater. Process. Technol. 213 (2013) 1327–1336. https://doi.org/10.1016/j.jmatprotec.2013.02.003.
[31] G. Molénat, L. Durand, J. Galy, A. Couret, Temperature control in spark plasma sintering: an FEM approach, J. Metall. 2010 (2010) 1–9. https://doi.org/10.1155/2010/145431.
[32] C. Manière, A. Pavia, L. Durand, G. Chevallier, K. Afanga, C. Estournès, Finite-element modeling of the electro-thermal contacts in the spark plasma sintering process, J. Eur. Ceram. Soc. 36 (2016) 741–748. https://doi.org/10.1016/j.jeurceramsoc.2015.10.033.
[33] M. Le Flem, A. Allemand, S. Urvoy, D. Cédat, C. Rey, Microstructure and thermal conductivity of Mo–TiC cermets processed by hot isostatic pressing, J. Nucl. Mater. 380 (2008) 85–92. https://doi.org/10.1016/j.jnucmat.2008.01.033.
[34] N. Durlu, Titanium carbide based composites for high temperature applications, J. Eur. Ceram. Soc. 19 (1999) 2415–2419. https://doi.org/10.1016/S0955-2219(99)00101-6.
[35] W.S. Williams, The thermal conductivity of metallic ceramics, JOM. 50 (1998) 62–66. https://doi.org/10.1007/s11837-998-0131-y.